

Received 23 July 2024, accepted 9 August 2024, date of publication 15 August 2024, date of current version 11 September 2024.

Digital Object Identifier 10.1109/ACCESS.2024.3444752



Blended Integral-Proportional/Proportional-Integral Control for Voltage Source Converter-Based AC Microgrids

CHIEBUKA EYISI[®], (Member, IEEE), AND QIFENG LI[®], (Senior Member, IEEE) Electrical and Computer Engineering Department, University of Central Florida, Orlando, FL 32816, USA

Corresponding author: Chiebuka Eyisi (cvpeyisi@ucf.edu)

This work was supported in part by the University of Central Florida (UCF) College of Graduate Studies Open Access Publishing Fund. The work of Qifeng Li was supported by U.S. National Science Foundation under Award ECCS 1808988.

ABSTRACT To allow a more effective utilization of distributed energy resources (DERs) in microgrids (MGs) and avoid violating operational limits of the asset, it is important that the stability and transient behavior or response of quantities such as voltages and currents is improved and maintained at appropriate levels. This paper uses small-signal analysis to investigate the behavior of blended integralproportional/proportional-integral (IPPI) voltage and current controllers by deriving state-space models and performing eigenvalue analysis in a voltage source converter-based microgrid (VSC-MG). The results are compared with conventional PI-based voltage and current controllers on the same VSC-MG, and show that by adjusting the blending factor for each VSC's IPPI-based voltage and current controllers, an improvement in stability and transient behavior can be achieved. An optimization framework based on particle swarm optimization is developed to aid in selecting blending factors for stable VSC-MG operation. Simulations are performed with the aid of MATLAB/Simulink to validate the theoretical analyses.

INDEX TERMS AC microgrid, boost converter, droop control, integral-proportional control, particle swarm optimization, proportional-integral control, small-signal analysis, voltage source converter.

I. INTRODUCTION

The interconnection between locally operated loads and one or more distributed energy resources (DERs), including energy storage systems (ESSs) and distributed generation (DGs), as an independent controllable entity is what constitutes a microgrid (MG) [1]. Two-stage power conversion structures consisting of DC-DC boost converter and DC-AC voltage source converter (VSC) subsystems can facilitate the integration of DERs such as ESSs or solar photovolatic systems (PVs) in MG networks, in which the low fluctuating output voltage of the resource is increased by the boost converter to a high regulated DC-link voltage fed to the VSC [2]. A voltage source converter-based microgrid (VSC-MG) operating in either islanded or grid-connected mode require control methods to aid in maintaining the operational limits

The associate editor coordinating the review of this manuscript and approving it for publication was Yifan Zhou.

of bus voltages, network frequency, and injected currents, while also improving their transient responses to system disturbances and preserving stability [3].

Instability in VSC-MGs can be caused by poorly tuned controllers, and until the controller is re-tuned, the system cannot be stabilized. A challenging issue for VSCs in relation to small-signal stability is the tuning of voltage and current controllers [4]. This becomes more challenging under varying operating conditions. The conventional proportional-integral (PI)-based control method is the most used control method in VSCs, incorporating an outer voltage controller and an inner current controller developed in a synchronously rotating d-q reference frame [5], [6]. In MG networks, stability assessment via small-signal analysis (eigenvalue, sensitivity, and participation factor analyses) requires appropriate state-space models of each component in the network [7]. In addition, stability assessment requires



inclusion of DC-side dynamics in the state-space modeling thereby introducing dynamic coupling between both VSC and boost converter subsystems [8].

In relation to preserving stability, an expansion of stability margins could translate to a higher degree of utilization and wider operating regions for the DER. Transients in VSC-MGs drive the system close to its operational limits which may cause these limits to be violated and potentially lead to instability. In PI controllers, the proportional and integral coefficients act on the error between the reference input command and the controlled output. However, the PI controller has a sluggish response, experiences a large overshoot, and is sensitive to the proportional and integral coefficients. Overshoots can lead to instability and stress components within the VSC-MG. In integral-proportional (IP) controllers, the integral coefficient acts on the error between the reference input command and the controlled output, while the proportional coefficient acts on the controlled output. Hence the IP controller is a two degree-of-freedom (2DOF) controller as the response to the input command and the response to the disturbance can be optimized independently. Initially introduced in [9], the IP controller has been used in [10] as a position controller for a synchronous motor and in [11] and [12] to improve the performance of DC and AC motor drives. Its also been used in [13] for DC-link voltage control in shunt active power filters and in [14] for rotor current control in doubly-fed induction generators. The IP controller overcame the drawbacks of the PI controller in these applications, particularly reducing the large overshoot. However, the IP controller experiences a large rise time, indicative of a slower response.

A PI controller designed for one operating condition may not perform well for another operating condition. For operating conditions close to operational limits, the problem of fast mitigation of transients becomes very important. A trade-off can be established by blending an IP controller with a PI controller to improve the performance of the disturbance rejection and input command tracking simultaneously, where both controllers are incorporated through a blending factor [15]. The blended integral-proportional/proportionalintegral (IPPI) controller combines the desirable attributes from both controllers and is incorporated in this paper to allow a more effective utilization of the VSC-interfaced DG and avoid violating its operational limits. This paper develops small-signal state-space models for blended IPPI voltage and current controllers, and investigates their behavior and small-signal stability in a VSC-MG. The results of the model are compared with the conventional PI-based voltage and current controllers on an islanded test VSC-MG network with DGs integrated through VSC and boost converter subsystems. The investigations within the paper

 The blended IPPI-based voltage and current controllers provides an added flexibility compared to the conventional PI-based voltage and current controllers in a VSC, allowing a more effective utilization. 2) The proposed objective function within an optimization framework is effective in selecting appropriate blending factors to enhance the damping characteristics and preserve stability for a desirable system performance.

The rest of the paper is organized as follows. Section II derives the small-signal state-space models for the blended IPPI voltage and current controllers. The VSC-MG model comprised of VSC and boost converter subsystems are presented in Section III. An optimization framework utilizing particle swarm optimization (PSO) through an objective function proposed to enhance damping characteristics is developed in Section IV. Small-signal stability analysis is performed on an islanded test VSC-MG network in Section V, and includes simulation results demonstrating the effectiveness of the optimization framework. Section VI concludes the paper.

II. THE PROPOSED BLENDED IPPI CONTROLLERS

The VSC subsystem spanning from its input terminals to the point of common coupling (PCC) is shown in the Fig. 1. Components within this subsystem include the VSC, the power controller, the virtual impedance model block, the inductor-capacitor-inductor (LCL) filter and dead-time model block, the digital control emulator (DCE) model block, and the inner IPPI current controller and outer IPPI voltage controller. The Figs. 2 and 3 representing the voltage and current controllers respectively, illustrate the application of the blending factor $\alpha \in [0, 1]$, where if $\alpha = 1$ results in a PI controller, whereas if $\alpha = 0$ results in an IP controller.

A. IPPI-BASED VOLTAGE CONTROLLER

The IPPI-based outer voltage controller is shown in Fig. 2 where the state and algebraic equations are

$$\dot{\phi}_d = v_{cd}^* - v_{cd}, \quad \dot{\phi}_q = v_{cq}^* - v_{cq}$$
 (1)

$$i_{id}^* = K_{iv}\phi_d + \alpha K_{pv}(v_{cd}^* - v_{cd}) - (1 - \alpha)K_{pv}v_{cd} - \omega_n C_f v_{cq} + F_C i_{gd}$$
 (2)

$$i_{iq}^* = K_{iv}\phi_q + \alpha K_{pv}(v_{cq}^* - v_{cq}) - (1 - \alpha)K_{pv}v_{cq} + \omega_n C_f v_{cd} + F_C i_{gq}$$
(3)

By linearizing and combining (1), (2), and (3), the corresponding state-space model is as shown:

$$\begin{bmatrix} \Delta \dot{\phi_d} \\ \Delta \dot{\phi_q} \end{bmatrix} = \underbrace{\begin{bmatrix} 0 & 0 \\ 0 & 0 \end{bmatrix}}_{A_{Vvsc}} \begin{bmatrix} \Delta \phi_d \\ \Delta \phi_q \end{bmatrix} + \underbrace{\begin{bmatrix} 1 & 0 \\ 0 & 1 \end{bmatrix}}_{B1_{Vvsc}} \begin{bmatrix} \Delta v_{cd}^* \\ \Delta v_{cq}^* \end{bmatrix} + \underbrace{\begin{bmatrix} -1 & 0 \\ 0 & -1 \end{bmatrix}}_{B2_{Vvsc}} \begin{bmatrix} \Delta v_{cd} \\ \Delta v_{cq} \end{bmatrix}$$

$$\begin{bmatrix} \Delta i_{id}^* \\ \Delta i_{iq}^* \end{bmatrix} = \underbrace{\begin{bmatrix} K_{iv} & 0 \\ 0 & K_{iv} \end{bmatrix}}_{Cver} \begin{bmatrix} \Delta \phi_d \\ \Delta \phi_q \end{bmatrix} + \underbrace{\begin{bmatrix} \alpha K_{pv} & 0 \\ 0 & \alpha K_{pv} \end{bmatrix}}_{D1_{v}} \begin{bmatrix} \Delta v_{cd}^* \\ \Delta v_{cq}^* \end{bmatrix}$$

$$(4)$$



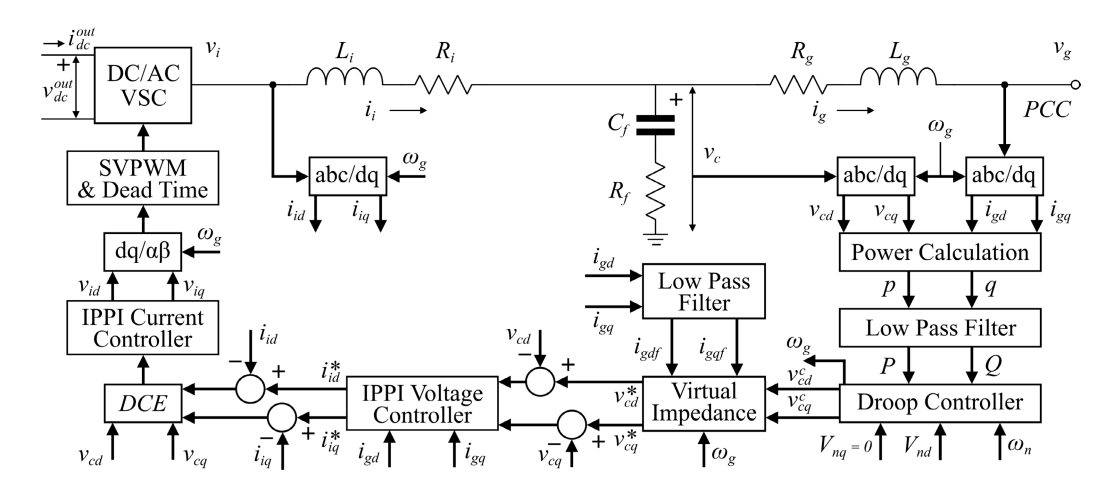


FIGURE 1. VSC Subsystem.

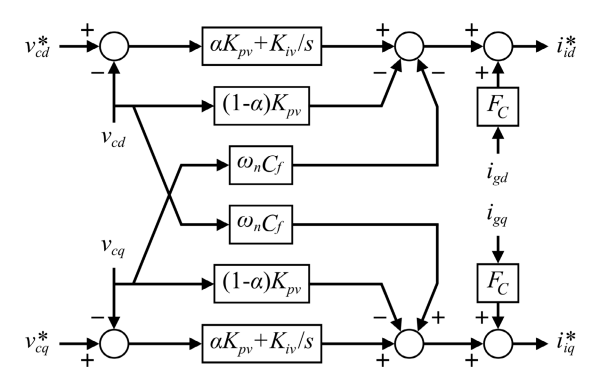


FIGURE 2. IPPI-Based Voltage Controller.

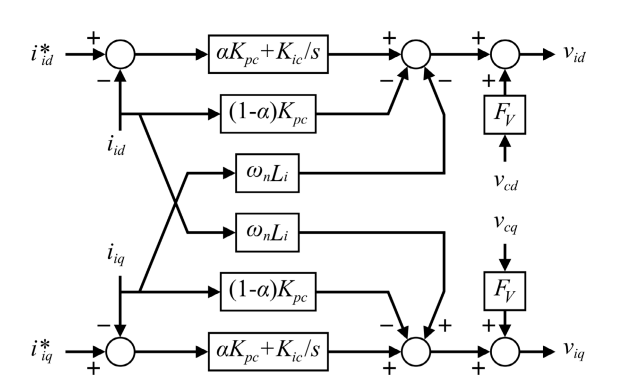


FIGURE 3. IPPI-Based Current Controller.

$$+\underbrace{\begin{bmatrix} -K_{pv} - \omega_n C_f \\ \omega_n C_f & -K_{pv} \end{bmatrix}}_{D2_{Vvsc}} \begin{bmatrix} \Delta v_{cd} \\ \Delta v_{cq} \end{bmatrix} + \underbrace{\begin{bmatrix} F_C & 0 \\ 0 & F_C \end{bmatrix}}_{D3_{Vvsc}} \begin{bmatrix} \Delta i_{gd} \\ \Delta i_{gq} \end{bmatrix}$$
(5)

where $\dot{\phi_{dq}}$ is the error between the measured output capacitor voltage v_{cdq} and the reference output capacitor voltage v_{cdq}^* in the d-q reference frame. The d-q components of the injected grid current and VSC output current reference are i_{gdq} and i_{idq}^* respectively. This voltage controller compares v_{cdq}^* with v_{cdq}

to generate i_{idq}^* . F_C is the feed-forward control gain of the injected grid current i_{gdq} . The nominal frequency operating point is ω_n . C_f models the filter capacitance of the LCL filter. The proportional and integral coefficients of the voltage controller are K_{pv} and K_{iv} respectively.

B. IPPI-BASED CURRENT CONTROLLER

The IPPI-based inner current controller is shown in Fig. 3 where the state and algebraic equations are

$$\dot{\gamma_d} = i_{id}^* - i_{id}, \quad \dot{\gamma_q} = i_{iq}^* - i_{iq}$$
 (6)

$$v_{id} = K_{ic}\gamma_d + \alpha K_{pc}(i_{id}^* - i_{id}) - (1 - \alpha)K_{pc}i_{id}$$
$$-\omega_n L_i i_{ia} + F_V v_{cd}$$
(7)

$$v_{iq} = K_{ic}\gamma_q + \alpha K_{pc}(i_{iq}^* - i_{iq}) - (1 - \alpha)K_{pc}i_{iq} + \omega_n L_i i_{id} + F_V v_{cq}$$
(8)

By linearizing and combining (6), (7), and (8), the corresponding state-space model is as shown:

$$\begin{bmatrix} \Delta \dot{\gamma}_{d} \\ \Delta \dot{\gamma}_{q} \end{bmatrix} = \underbrace{\begin{bmatrix} 0 & 0 \\ 0 & 0 \end{bmatrix}}_{A_{Cysc}} \begin{bmatrix} \Delta \gamma_{d} \\ \Delta \gamma_{q} \end{bmatrix} + \underbrace{\begin{bmatrix} 1 & 0 \\ 0 & 1 \end{bmatrix}}_{B1_{Cysc}} \begin{bmatrix} \Delta i_{id}^{*} \\ \Delta i_{iq}^{*} \end{bmatrix} + \underbrace{\begin{bmatrix} -1 & 0 \\ 0 & -1 \end{bmatrix}}_{B2_{Cysc}} \begin{bmatrix} \Delta i_{id} \\ \Delta i_{iq} \end{bmatrix}$$

$$= \underbrace{\begin{bmatrix} K_{ic} & 0 \\ 0 & K_{ic} \end{bmatrix}}_{C_{Cysc}} \begin{bmatrix} \Delta \gamma_{d} \\ \Delta \gamma_{q} \end{bmatrix} + \underbrace{\begin{bmatrix} \alpha K_{pc} & 0 \\ 0 & \alpha K_{pc} \end{bmatrix}}_{D1_{Cysc}} \begin{bmatrix} \Delta i_{id}^{*} \\ \Delta i_{iq}^{*} \end{bmatrix} + \underbrace{\begin{bmatrix} -K_{pc} & -\omega_{n}L_{i} \\ \omega_{n}L_{i} & -K_{pc} \end{bmatrix}}_{D2_{Cysc}} \begin{bmatrix} \Delta i_{id} \\ \Delta i_{iq} \end{bmatrix} + \underbrace{\begin{bmatrix} F_{V} & 0 \\ 0 & F_{V} \end{bmatrix}}_{D3_{Cysc}} \begin{bmatrix} \Delta v_{cd} \\ \Delta v_{cq} \end{bmatrix}$$

where $\dot{\gamma_{dq}}$ is the error between the measured VSC output current i_{idq} and the reference VSC output current i_{idq}^* in the d-q reference frame. The d-q components of the



output capacitor voltage and VSC output voltage are v_{cdq} and v_{idq} respectively. This current controller compares i_{idq}^* with i_{idq} to generate v_{idq} . F_V is the feed-forward control gain of the output capacitor voltage v_{cdq} . L_i models the VSC-side inductance of the LCL filter. The proportional and integral coefficients of the current controller are K_{pc} and K_{ic} respectively.

C. BENEFITS FROM BLENDING IP AND PI CONTROLLERS

Consider a plant G(s) = N(s)/D(s) in the block diagram shown in Fig. 4 where both IP and PI controllers are incorporated through a blending factor $\alpha \in [0, 1]$. The closed-loop transfer function between the output Y(s) and reference input $Y_r(s)$ is

$$\frac{Y(s)}{Y_r(s)} = \frac{\left(\alpha K_p s + K_i\right) N(s)}{s D(s) + \left(K_p s + K_i\right) N(s)} \tag{11}$$

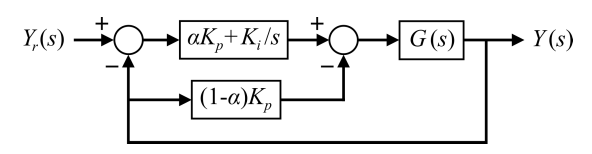


FIGURE 4. IPPI Control Loop.

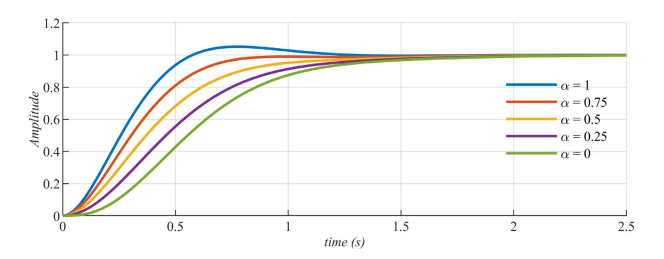


FIGURE 5. Step Response Characteristics.

The step response of (11) shown in Fig. 5 for $K_p =$ 30 and $K_i = 80$, illustrates a larger overshoot with PI ($\alpha =$ 1) control and a slower response with IP ($\alpha = 0$) control when working alone. The PI controller by introducing zeros causes the overshoot. The overshoot can be eliminated by the IP controller that does not introduce zeros. For fixed pole locations, the closer the zeros are to the origin of the complex plane, the larger the effect on dynamic performance related to overshoot. The feedback of $(1 - \alpha)K_p$ provides an active damping like term that improves the stability of the system. Combining both controllers through an appropriately selected blending factor (e.g. $\alpha = 0.75$) aids in moving the controller zeros further to the left of the complex plane thereby minimizing overshoot and also aids in moving system poles to more convenient locations for a desired system response through matrices $D1_{Vvsc}$ and $D1_{Cvsc}$. In a similar manner to PI controllers with setpoint weighting, the blended IPPI controllers offer a much better solution than traditional ways of de-tuning the PI controller [16]. This paper illustrates the blended IPPI controllers, albeit similar to PI controllers with setpoint weighting, as newly applied to VSCs and

aided by a proposed optimization framework for a desirable system performance.

III. STATE-SPACE MODEL OF A GENERIC VSC-MG

Small-signal state-space models are developed from the linearizarion of mathematical equations describing system dynamics, around stable operating points. In the investigated VSC-MG, this is inclusive of state-space models for both VSC and boost converter subsystems, and interconnected lines and loads. Dead-time effect [17], and the effect of the digital controller's time delay [18], are also incorporated. The graphical modeling approach in [19] is adopted in the small-signal state-space modeling of the VSC-MG.

A. VSC SUBSYSTEM STATE-SPACE MODELING

The state-space models shown within this subsection for the power controller, LCL filter with dead-time effect, virtual impedance, VSC DCE, and reference frame transformation are available in [5] and [19] with more detailed information. The state-space model of the power controller is as shown in (12)–(13), where p and q are instantaneous active and reactive power outputs of the VSC with low-pass filtered steady-state values P and Q respectively. This filter's cutoff frequency is ω_{cpc} . V_{ndq} is the nominal voltage operating point in the d-q reference frame. The difference in phase angle between a common reference frame rotating at ω_{gcom} and an individual VSC's reference frame is δ . Droop gains are set by m_p (in rad/s/W) and n_q (in V/Var) for active and reactive power respectively. The d-q components of the injected grid current and output capacitor voltage are i_{gdq} and v_{cdq} , with corresponding steady-state values I_{gdq} and V_{cdq} respectively. In the individual VSC, the droop-governed frequency is ω_g , whereas the droop-governed command output capacitor voltage is v_{cdq}^c .

$$\begin{bmatrix} \Delta \dot{\delta} \\ \Delta \dot{P} \\ \Delta \dot{Q} \end{bmatrix} = \underbrace{\begin{bmatrix} 0 & -m_p & 0 \\ 0 & -\omega_{cpc} & 0 \\ 0 & 0 & -\omega_{cpc} \end{bmatrix}}_{A_{Pvsc}} \begin{bmatrix} \Delta \delta \\ \Delta P \\ \Delta Q \end{bmatrix} + \underbrace{\begin{bmatrix} -1 \\ 0 \\ 0 \end{bmatrix}}_{B2_{Pvsc}} [\Delta \omega_{gcom}]$$

$$+ \frac{3}{2} \omega_{cpc} \underbrace{\begin{bmatrix} 0 & 0 & 0 & 0 \\ I_{gd} & I_{gq} & V_{cd} & V_{cq} \\ -I_{gq} & I_{gd} & V_{cq} - V_{cd} \end{bmatrix}}_{B1_{Pvsc}} \begin{bmatrix} \Delta^{vcd} \\ \Delta^{vcq} \\ \Delta^{i}_{gd} \\ \Delta^{i}_{gq} \end{bmatrix}$$

$$\begin{bmatrix} \Delta \omega_{g} \\ \Delta v_{cq}^{c} \\ \Delta v_{cq}^{c} \end{bmatrix} = \underbrace{\begin{bmatrix} 0 & -m_p & 0 \\ 0 & 0 & -n_q \\ 0 & 0 & 0 \end{bmatrix}}_{C_{P}} \begin{bmatrix} \Delta \delta \\ \Delta P \\ \Delta Q \end{bmatrix}$$

$$(13)$$

The state-space model of the LCL filter incorporating dead-time effect with continuous space vector pulse width modulation (SVPWM) [17] is as shown in (15)–(18), at the bottom of the next page. where k_d in (17) is

$$k_d = \frac{1}{L_i} \frac{T_d}{T_{sw}} \frac{2\sqrt{6}}{\pi} \frac{1}{\left(I_{id}^2 + I_{iq}^2\right)^{3/2}}$$
(14)



where i_{idq} , i_{gdq} , v_{idq} , and v_{cdq} remain as previously described. Their corresponding steady-state values are I_{idq} , I_{gdq} , V_{idq} , and V_{cdq} respectively. The switching period and dead-time are $T_{sw} = 1/f_{sw}$ and T_d respectively. The d-q components of the VSC's grid-bus voltage at the PCC and its corresponding steady-state value are v_{gdq} and V_{gdq} respectively. The output voltage of the associated boost converter and its corresponding steady-state value are v_{dc}^{out} and V_{dc}^{out} respectively. The LCL filter parameters R_g and L_g , C_f and R_f , and L_i and R_i model the grid-bus-side inductance, filter capacitance, and VSC-side inductance respectively.

The state-space model of the virtual impedance block [20] is as shown in (19)–(20), where the virtual inductance and resistance are L_v and R_v respectively. The d-q components of the injected grid current and its low-pass filtered values are i_{gdq} and i_{gdqf} respectively, with corresponding steady-state value $I_{gdqf} = I_{gdq}$. This filter's cut-off frequency is ω_{cvi} . The d-q components of the droop-governed command output capacitor voltage and the reference output capacitor voltage are v_{cdq}^c and v_{cdq}^* respectively.

$$\begin{bmatrix}
\Delta i_{gdf} \\
\Delta i_{gqf}
\end{bmatrix} = \underbrace{\begin{bmatrix}
-\omega_{cvi} & 0 \\
0 & -\omega_{cvi}
\end{bmatrix}}_{A_{virt}} \begin{bmatrix}
\Delta i_{gdf} \\
\Delta i_{gqf}
\end{bmatrix} \\
+ \underbrace{\begin{bmatrix}
\omega_{cvi} & 0 \\
0 & \omega_{cvi}
\end{bmatrix}}_{B_{virt}} \begin{bmatrix}
\Delta i_{gd} \\
\Delta i_{gq}
\end{bmatrix}$$

$$\begin{bmatrix}
\Delta v_{cd}^* \\
\Delta v_{cq}^*
\end{bmatrix} = \underbrace{\begin{bmatrix}
-R_v & L_v \omega_n \\
L_v \omega_n & -R_v
\end{bmatrix}}_{C_{virt}} \begin{bmatrix}
\Delta i_{gdf} \\
\Delta i_{gqf}
\end{bmatrix} \\
+ \underbrace{\begin{bmatrix}
1 & 0 \\
0 & 1
\end{bmatrix}}_{C_{virt}} \begin{bmatrix}
\Delta v_{cd}^c \\
\Delta v_{cq}^c
\end{bmatrix}}_{D_{virt}} + \underbrace{\begin{bmatrix}
L_v I_{gqf} \\
-L_v I_{gdf}
\end{bmatrix}}_{D_{virt}} \begin{bmatrix}
\Delta \omega_g
\end{bmatrix}$$

$$(20)$$

The state-space model of the VSC's DCE, modeling its digital implementation [21] as shown in (21), follows the Padé approximation illustrated in [16]. This is applied to all input signals $(v_{cdq}, i_{idq}, \text{ and } i_{idq}^*)$ to the VSC's current controller. T_s is the sampling period delay.

$$G_{DCE}(s) = e^{-sT_s} \frac{1}{T_c} \frac{1 - e^{-sT_s}}{s}$$
 (21)

The reference frame transformation using one of the VSC's synchronous reference frame as the common D-Q reference frame with frequency $\omega_g = \omega_{gcom}$ [5], in which all other individual VSCs in the network are transformed to is as shown in (22)–(23). In the common *D-Q* reference frame, the steady-state values of the individual VSC's injected grid current and grid-bus voltage at the PCC are I_{gDQ} and V_{gDO} respectively. The phase angle difference between an individual VSC's d-q reference frame and the common D-Qreference frame is δ and its corresponding steady-state value

$$\begin{bmatrix} \Delta i_{gD} \\ \Delta i_{gQ} \end{bmatrix} = \begin{bmatrix} \cos(\delta_0) - \sin(\delta_0) \\ \sin(\delta_0) & \cos(\delta_0) \end{bmatrix} \begin{bmatrix} \Delta i_{gd} \\ \Delta i_{gq} \end{bmatrix}$$

$$+ \begin{bmatrix} -I_{gd} \sin(\delta_0) - I_{gq} \cos(\delta_0) \\ I_{gd} \cos(\delta_0) - I_{gq} \sin(\delta_0) \end{bmatrix} [\Delta \delta]$$

$$\begin{bmatrix} \Delta v_{gd} \\ \Delta v_{gq} \end{bmatrix} = \begin{bmatrix} \cos(\delta_0) & \sin(\delta_0) \\ -\sin(\delta_0) & \cos(\delta_0) \end{bmatrix} \begin{bmatrix} \Delta v_{gD} \\ \Delta v_{gQ} \end{bmatrix}$$

$$+ \begin{bmatrix} -V_{gD} \sin(\delta_0) + V_{gQ} \cos(\delta_0) \\ -V_{gD} \cos(\delta_0) - V_{gQ} \sin(\delta_0) \end{bmatrix} [\Delta \delta]$$
(23)

B. BOOST CONVERTER SUBSYSTEM STATE-SPACE **MODELING**

The boost converter subsystem spanning from its input terminals to the input terminals of the VSC subsystem is shown in the Fig. 6. Components within this subsystem include the boost converter power model, the digital control

$$\begin{bmatrix} x_{icl} \end{bmatrix} = A_{lcl} \begin{bmatrix} \Delta x_{lcl} \end{bmatrix} + B1_{lcl} \begin{bmatrix} \Delta v_{id} \\ \Delta v_{iq} \end{bmatrix} + B2_{lcl} \begin{bmatrix} \Delta v_{gd} \\ \Delta v_{gq} \end{bmatrix} + B3_{lcl} \begin{bmatrix} \Delta \omega_g \end{bmatrix}$$

$$\begin{bmatrix} x_{icl} \end{bmatrix} = \begin{bmatrix} \Delta i_{id} \quad \Delta i_{iq} \quad \Delta i_{gd} \quad \Delta i_{gq} \quad \Delta v_{cd} \quad \Delta v_{cq} \end{bmatrix}, \quad \begin{bmatrix} x_{lcl} \end{bmatrix} = \begin{bmatrix} \Delta i_{id} \quad \Delta i_{iq} \quad \Delta i_{gd} \quad \Delta i_{gq} \quad \Delta v_{cd} \quad \Delta v_{cq} \end{bmatrix}$$

$$\begin{bmatrix} -\frac{R_i}{L_i} - k_d I_{iq}^2 V_{dc}^{out} & \omega_n + k_d I_{id} I_{iq} V_{dc}^{out} & 0 & 0 & -\frac{1}{L_i} & 0 \\ -\omega_n + k_d I_{id} I_{iq} V_{dc}^{out} & -\frac{R_i}{L_i} - k_d I_{id}^2 V_{dc}^{out} & 0 & 0 & 0 & -\frac{1}{L_i} \end{bmatrix}$$

$$(15)$$

$$\begin{bmatrix}
-\frac{R_{i}}{L_{i}} - k_{d}I_{iq}^{2}V_{dc}^{out} & \omega_{n} + k_{d}I_{id}I_{iq}V_{dc}^{out} & 0 & 0 & -\frac{1}{L_{i}} & 0 \\
-\omega_{n} + k_{d}I_{id}I_{iq}V_{dc}^{out} & \omega_{n} + k_{d}I_{id}I_{iq}V_{dc}^{out} & 0 & 0 & 0 & -\frac{1}{L_{i}} \\
0 & 0 & -\frac{R_{g}}{L_{i}} - k_{d}I_{id}^{2}V_{dc}^{out} & -\frac{R_{i}}{L_{i}} - k_{d}I_{id}^{2}V_{dc}^{out} & 0 & 0 & 0 & -\frac{1}{L_{i}} \\
0 & 0 & -\frac{R_{g}}{L_{g}} & \omega_{n} & \frac{1}{L_{g}} & 0 \\
0 & 0 & -\omega_{n} & -\frac{R_{g}}{L_{g}} & 0 & \frac{1}{L_{g}} \\
\frac{1}{C_{f}} - \frac{R_{f}R_{i}}{L_{i}} - R_{f}k_{d}I_{iq}^{2}V_{dc}^{out} & R_{f}k_{d}I_{id}I_{iq}V_{dc}^{out} & \frac{R_{f}R_{g}}{L_{g}} - \frac{1}{C_{f}} & 0 & -\frac{R_{f}}{L_{i}} - \frac{R_{f}}{L_{g}} & \omega_{n} \\
R_{f}k_{d}I_{id}I_{iq}V_{dc}^{out} & \frac{1}{C_{f}} - \frac{R_{f}R_{i}}{L_{i}} - R_{f}k_{d}I_{id}^{2}V_{dc}^{out} & 0 & \frac{R_{f}R_{g}}{L_{g}} - \frac{1}{C_{f}} & -\omega_{n} & -\frac{R_{f}}{L_{i}} - \frac{R_{f}}{L_{g}}
\end{bmatrix}$$

$$(16)$$

$$\underbrace{\begin{bmatrix} \frac{1}{L_{i}} & 0 & 0 & 0 & \frac{R_{f}}{L_{i}} & 0 \\ 0 & \frac{1}{L_{i}} & 0 & 0 & 0 & \frac{R_{f}}{L_{i}} \end{bmatrix}^{T}}_{B1_{lcl}}, \quad \underbrace{\begin{bmatrix} 0 & 0 & -\frac{1}{L_{g}} & 0 & \frac{R_{f}}{L_{g}} & 0 \\ 0 & 0 & -\frac{1}{L_{g}} & 0 & \frac{R_{f}}{L_{g}} \end{bmatrix}^{T}}_{B2_{lcl}}, \quad \underbrace{\begin{bmatrix} I_{iq} & -I_{id} & I_{gq} & -I_{gd} & V_{cq} & -V_{cd} \end{bmatrix}^{T}}_{B3_{lcl}} \tag{18}$$



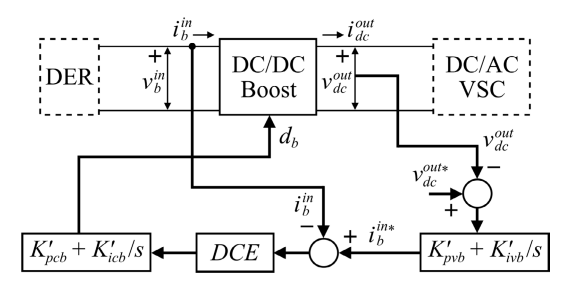


FIGURE 6. Boost converter subsystem.

emulator (DCE) model block, and the inner PI current controller and outer PI voltage controller. The state-space models shown within this subsection are available in [19] and [22] with more detailed information.

The state-space model of the PI-based outer voltage controller is as shown in (24)–(25), where $\dot{\phi}_b$ is the error between the measured DC-link output voltage v_{dc}^{out} and the reference DC-link output voltage v_{dc}^{out*} . The boost converter's input current reference is i_b^{in*} . This voltage controller compares v_{dc}^{out*} with v_{dc}^{out} to generate i_b^{in*} . The proportional and integral coefficients of the voltage controller are K'_{pvb} and K'_{ivb} respectively.

$$\begin{bmatrix} \Delta \dot{\phi_b} \end{bmatrix} = \underbrace{\begin{bmatrix} 0 \end{bmatrix}}_{A_{Vb}} \begin{bmatrix} \Delta \phi_b \end{bmatrix} + \underbrace{\begin{bmatrix} 1 \end{bmatrix}}_{B1_{Vb}} \begin{bmatrix} \Delta v_{dc}^{out*} \end{bmatrix} + \underbrace{\begin{bmatrix} -1 \end{bmatrix}}_{B2_{Vb}} \begin{bmatrix} \Delta v_{dc}^{out} \end{bmatrix} (24)$$

$$\begin{bmatrix} \Delta i_b^{in*} \end{bmatrix} = \underbrace{\begin{bmatrix} K'_{ivb} \end{bmatrix}}_{C_{Vb}} \begin{bmatrix} \Delta \phi_b \end{bmatrix} + \underbrace{\begin{bmatrix} K'_{pvb} \end{bmatrix}}_{D1_{Vb}} \begin{bmatrix} \Delta v_{dc}^{out*} \end{bmatrix}$$

$$+ \underbrace{\begin{bmatrix} -K'_{pvb} \end{bmatrix}}_{D2_{Vb}} \begin{bmatrix} \Delta v_{dc}^{out} \end{bmatrix} (25)$$

The state-space model of the PI-based inner current controller is as shown in (26)–(27), where $\dot{\gamma}_b$ is the error between the measured input current i_b^{in} and the reference input current i_b^{in*} . The boost converter's duty cycle is d_b . This current controller compares i_b^{in*} with i_b^{in} to generate d_b . The proportional and integral coefficients of the current controller are K'_{pcb} and K'_{icb} respectively.

$$[\Delta \dot{\gamma}_{b}] = \underbrace{\begin{bmatrix} 0 \end{bmatrix}}_{A_{Cb}} [\Delta \gamma_{b}] + \underbrace{\begin{bmatrix} 1 \end{bmatrix}}_{B1_{Cb}} [\Delta i_{b}^{in*}] + \underbrace{\begin{bmatrix} -1 \end{bmatrix}}_{B2_{Cb}} [\Delta i_{b}^{in}]$$
(26)
$$[\Delta d_{b}] = \underbrace{\begin{bmatrix} K'_{icb} \end{bmatrix}}_{C_{Cb}} [\Delta \gamma_{b}] + \underbrace{\begin{bmatrix} K'_{pcb} \end{bmatrix}}_{D1_{Cb}} [\Delta i_{b}^{in*}] + \underbrace{\begin{bmatrix} -K'_{pcb} \end{bmatrix}}_{D2_{Cb}} [\Delta i_{b}^{in}]$$
(27)

The state-space model of the power model (Fig. 7) is as shown in (28)–(29), where R_{lb} and L_{lb} are the internal resistance and inductance of the input filter inductor respectively, C_{dc} is the capacitance of the output DC-link capacitor, and R_{onb} is the resistance of the switching device in its "on-state". PI-based voltage and current controllers are often used in DC-DC boost converters in comparison with advanced control methods [23], and not in the scope of this paper. Moreover, some dominant modes in an islanded VSC-MG network were shown in [24] to be more sensitive

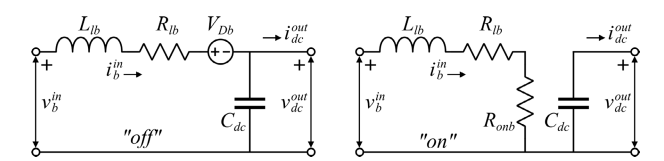


FIGURE 7. Boost Converter Power Model.

to states belonging to the boost converter's power model and not sensitive to states belonging to its accompanying PI-based voltage and current controllers. Hence requiring the parameters R_{lb} , L_{lb} , and R_{onb} be carefully selected. Consequently, the blending of IP and PI controllers is not considered for the boost converter. The boost converter's duty cycle and the diode's forward voltage drop are d_b and V_{Db} respectively. The input and output currents are i_b^{in} and i_{dc}^{out} , whereas the input and output voltages are v_b^{in} and v_{dc}^{out} . The steady-state values of the input current, the output voltage, and the duty cycle of the boost converter are I_b^{in} , V_{dc}^{out} , and D_b respectively.

$$\begin{bmatrix} \Delta i_{b}^{in} \\ \Delta v_{dc}^{out} \end{bmatrix} = \underbrace{\begin{bmatrix} \frac{-R_{lb} - D_{b}R_{onb}}{L_{lb}} & \frac{-1 + D_{b}}{L_{lb}} \\ \frac{1 - D_{b}}{C_{dc}} & 0 \end{bmatrix}}_{A_{Pb}} \begin{bmatrix} \Delta i_{b}^{in} \\ \Delta v_{dc}^{out} \end{bmatrix} + \underbrace{\begin{bmatrix} \frac{1}{L_{lb}} \\ 0 \end{bmatrix}}_{B1_{Pb}} [\Delta v_{b}^{in}]$$

$$+ \underbrace{\begin{bmatrix} \frac{V_{dc}^{out} + V_{Db} - R_{onb}I_{b}^{in}}{L_{lb}} \\ -\frac{I_{b}^{in}}{C_{dc}} \end{bmatrix}}_{B2_{Pb}} [\Delta d_{b}] + \underbrace{\begin{bmatrix} 0 \\ -\frac{1}{C_{dc}} \end{bmatrix}}_{B3_{Pb}} [\Delta i_{dc}^{out}]$$

$$(28)$$

$$\begin{bmatrix} \Delta i_b^{in} \\ \Delta v_{dc}^{out} \end{bmatrix} = \underbrace{\begin{bmatrix} 1 & 0 \\ 0 & 1 \end{bmatrix}}_{C_{Pb}} \begin{bmatrix} \Delta i_b^{in} \\ \Delta v_{dc}^{out} \end{bmatrix} + \underbrace{\begin{bmatrix} 0 & 0 & 0 \\ 0 & 0 & 0 \end{bmatrix}}_{D_{Pb}} \begin{bmatrix} \Delta v_b^{in} \\ \Delta d_b \end{bmatrix}$$
(29)

The DCE is applied and approximated in a similar way as with the VSC subsystem to all input signals (i_b^{in} and i_b^{in*}) to the boost converter's current controller.

C. LINKING THE VSC AND BOOST CONVERTER SUBSYSTEMS

The state-space model linking both VSC and boost converter subsystems [19] is as shown in (30)–(31), where v_{idq} and v_{dc}^{out} are linked through the d-q components of the VSC's duty cycle d_{dq} , with corresponding steady-state value D_{dq} , whereas i_{dc}^{out} and i_{idq} are linked through the power balance principle equating the VSC's output active power to the active power in the DC-link.

$$\begin{bmatrix} \Delta v_{id} \\ \Delta v_{iq} \end{bmatrix} = \underbrace{\begin{bmatrix} D_d \\ D_q \end{bmatrix}}_{C_{Vlink}} \begin{bmatrix} \Delta v_{dc}^{out} \end{bmatrix} + \underbrace{\begin{bmatrix} V_{dc}^{out} & 0 \\ 0 & V_{dc}^{out} \end{bmatrix}}_{D_{Vlink}} \begin{bmatrix} \Delta d_d \\ \Delta d_q \end{bmatrix}$$
(30)

$$\left[\Delta i_{dc}^{out}\right] = \frac{3}{2} \underbrace{\left[D_{d} \ D_{q}\right]}_{C_{Clink}} \begin{bmatrix} \Delta i_{id} \\ \Delta i_{iq} \end{bmatrix} + \frac{3}{2} \underbrace{\left[I_{id} \ I_{iq}\right]}_{D_{Clink}} \begin{bmatrix} \Delta d_{d} \\ \Delta d_{q} \end{bmatrix}$$
(31)



D. LINE, LOAD, AND COMPLETE VSC-MG NETWORK STATE-SPACE MODELING

The state-space models of a generic RL line and RL load are available in [5] with more detailed information and not repeated here. The complete VSG-MG network state-space model is as shown in (33), and is as a result of introducing a virtual resistor R_N as shown in (32) through matrices M_{VSC} , M_{LN} , and M_{LD} , mapping the VSCs, lines, and loads respectively to each bus in the network. The state-space model of all interconnecting lines and loads in the VSC-MG network are $[i_{LNDQ}]$ and $[i_{LDDQ}]$ respectively [5], [6].

$$\left[\Delta v_{gDQ} \right] = R_N \left(M_{VSC} \left[\Delta i_{gDQ} \right] + M_{LN} \left[\Delta i_{LNDQ} \right] + M_{LD} \left[\Delta i_{LDDQ} \right] \right)$$
 (32)

$$\begin{bmatrix} \Delta x_{BCVSC} \\ \Delta i_{LNDQ} \\ \Delta i_{LDDQ} \end{bmatrix} = A_{MG} \begin{bmatrix} \Delta x_{BCVSC} \\ \Delta i_{LNDQ} \\ \Delta i_{LDDQ} \end{bmatrix}$$
(33)

The lines, loads, and VSC and boost converter subsystems are combined using the graphical modeling approach in [19] to construct the complete system state matrix A_{MG} . For the *i*th DG, the state vector x_{BCVSC} containing all associated states in the VSC and boost converter subsystems is as shown in (34).

$$\Delta x_{BCVSCi} = \Delta \left[\phi_{bi} \ \gamma_{bi} \ i_{bi}^{in} \ v_{dci}^{out} \right]$$
$$\delta_{i} \ P_{i} \ Q_{i} \ i_{gdqfi} \ \phi_{dqi} \ \gamma_{dqi} \ i_{idqi} \ i_{gdqi} \ v_{cdqi} \right]^{T}$$
(34)

IV. OPTIMIZATION OF THE BLENDING FACTOR

Particle swarm optimization (PSO) forms the basis to which an optimization framework is developed in this section due to its convergence capability and simplicity of tuning parameters [25]. Inspired by the swarm intelligence concept, it has an easy implementation and an effective memory capability. Particles in the swarm are subject to velocities within the search space using the swarm's best experience and its own best knowledge as shown in (35)–(37), where k, i, and N are the iteration index, the particle, and the total number of iterations set to 50 respectively. The total number of particles in the swarm p_s is set to 5. At iteration k, the inertia weight w^k decreases linearly from w_{max} to w_{min} with settings 0.9 to 0.4 respectively, whereas the velocity and position vectors for each particle i are V_i^k and X_i^k respectively. The constants c_1 , c_2 are positive numbers set to 2, and r_1 , r_2 are two uniformly distributed random numbers in the range [0, 1]. The second and third components in (36) scaled by c_1r_1 and c_2r_2 represent the "self-knowledge" and "group-knowledge" components of each particle respectively. During the iterative process, the best positions each particle i has attained based on its own knowledge and the swarm's best experience are Xpb_i^k and Xsb^k respectively.

$$w^{k} = w_{max} - (w_{max} - w_{min}) \cdot ((k-1)/N)$$
(35)

$$V_i^{k+1} = w^k V_i^k + c_1 r_1 (X p b_i^k - X_i^k) + c_2 r_2 (X s b^k - X_i^k)$$
 (36)

$$X_i^{k+1} = X_i^k + V_i^{k+1} (37)$$

This tool is used to obtain an appropriate blending factor in the scenario where PI controllers are unable to preserve stability, by moving the dominant modes in the system to their furthest possible locations from the right half of the complex plane. A mode in the form $m_y = \sigma$ or $m_y^x = \sigma \pm j\omega$ has a frequency of oscillation $f = \omega/2\pi$, and damping ratio $\zeta = -\sigma/\sqrt{\sigma^2 + \omega^2}$. An improved stable overall system performance is attainable when the dominant modes are moved further to the left of the complex plane. The objective function expressed in (38) at its minimum would indicate that all dominant modes in the system are at their furthest possible locations from the right half of the complex plane.

$$\min_{\alpha} J = \sum_{m=1}^{M} \sigma_m$$
s.t. $0 \le \alpha_n \le 1 \quad (n = 1, 2, ..., N)$

$$\sigma_0 \le \sigma_m \le 0 \quad (m = 1, 2, ..., M)$$

$$\zeta_0 \le \zeta_m \tag{38}$$

where α_n represents the blending factors of the IPPI controllers for the nth VSC. The conditions $\sigma_0 \leq \sigma_m \leq 0$ and $\zeta_0 \leq \zeta_m$ are imposed simultaneously to have some degree of relative stability and limit the maximum overshoot respectively, where M is the number of modes, σ_m and ζ_m are the real part and damping ratios of the mth mode respectively, and σ_0 and ζ_0 are the corresponding desirable performance metrics. To facilitate the convergence of the swarm, the conditions in (39) and (40) are performed at every iteration after each particle's velocity and position are updated.

$$\begin{split} X_{i,j}^{max} &= \max \left[X_{i,j} \right], \ X_{i,j}^{min} = \min \left[X_{i,j} \right] \\ &\text{if } X_{i,j}^k > X_{i,j}^{max}, \ \text{then } X_{i,j}^k = X_{i,j}^{max} \\ &\text{else if } X_{i,j}^k < X_{i,j}^{min}, \ \text{then } X_{i,j}^k = X_{i,j}^{min} \\ &V_{i,j}^{max} = 0.2 \left(X_{i,j}^{max} - X_{i,j}^{min} \right), \ V_{i,j}^{min} = -V_{i,j}^{max} \\ &\text{if } V_{i,j}^k > V_{i,j}^{max}, \ \text{then } V_{i,j}^k = V_{i,j}^{max} \end{aligned} \tag{40}$$
 else if $V_{i,j}^k < V_{i,j}^{min}, \ \text{then } V_{i,j}^k = V_{i,j}^{min}$

where $X_{i,j}^{max}$ and $X_{i,j}^{min}$ are the upper and lower limits with regards to the domain of stability for the *j*th element of the *i*th particle's position $X_{i,j}$, whereas $V_{i,j}^{max}$ and $V_{i,j}^{min}$ are the upper and lower limits with regards to the *j*th element of the *i*th particle's velocity $V_{i,j}$. The following steps describe the complete optimization framework using PSO.

1) Initialization:

- 1.1 In the swarm of size p_s , randomly select each particle's position $X_{i,j}$ within the domain of stability.
- 1.2 Initialize each particle's velocity $V_{i,j}$ to 0.
- 1.3 Evaluate overall system modes for each particle.
- 1.4 Evaluate J using (38) for each particle. Xpb_i is initialized with a copy of X_i , whereas Xsb is initialized with a copy of X_i having the best J.
- 2) *Iteration & Weight Update*: With *k* starting at 1, update the iteration index. Update the inertia weight using (35).



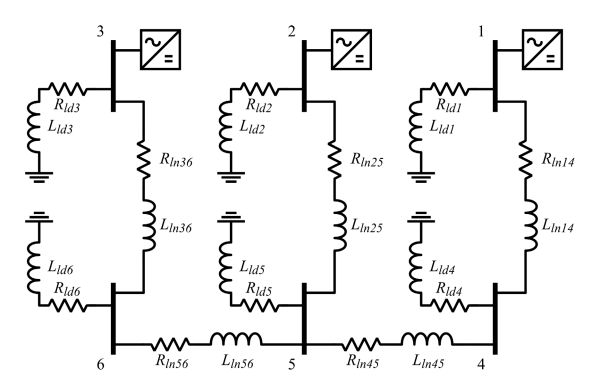


FIGURE 8. Test VSC-MG Network.

- 3) *Velocity Update*: Update each particle's velocity using (36). Then apply (40) to ensure all velocities are within predefined limits.
- 4) *Position Update*: With the updated velocities, each particle's position is updated using (37). Then apply (39) to ensure all positions are within predefined limits.
- 5) *Objective Function Evaluation*: For each particle, evaluate overall system modes. Then evaluate *J* using (38).
- 6) Particle Best Update: For each particle, if the evaluated J in current iteration is better than the evaluated J's in previous iterations, then update Xpb_i with a copy of X_i .
- 7) Swarm Best Update: In current iteration, update Xsb with a copy of Xpb_i having the best J.
- 8) *Stopping Criteria*: Repeat steps 2 to 7 until one of the following conditions is met:
 - 8.1 The evaluated *J* has not improved for a predefined number of iterations.
 - 8.2 The maximum number of iterations N is reached.

V. SMALL-SIGNAL STABILITY ANALYSIS ON TEST VSC-MG NETWORK

An islanded 50 Hz, 230 V VSC-MG network shown in the Fig. 8 consists of DGs represented in a two-stage power conversion structure comprised of VSC and boost converter subsystems. Tables 1 and 2 show the parameters and steady-state initial operating conditions respectively in the MG network, similar to [19]. DGs in the network are rated at 100 kVA. With the aid of MATLAB/Simulink R2018b, stability is assessed using the small-signal state-space models described in Sections II and III.

A. MODAL ANALYSIS

The complete state-space model of the VSC-MG network in Fig. 8 has a total of 245 states, and the DG's VSC at bus 1 is selected as the common reference frame to which other VSCs are transformed to. For the blended IPPI voltage and current controllers described in Section II, if $\alpha=1$ the controllers become PI controllers, whereas if $\alpha=0$ the controllers become IP controllers. Table 3 shows certain eigenvalues (modes) of interest due to the proximity of their trajectories to the right half of the complex plane as α changes. This

TABLE 1. VSC, boost converter, and network model parameters.

Par.	Value	Par.	Value	Par.	Value
V_n	230 V	f_{sw}	10 kHz	T_d	2 μs
ω_n, ω_g	100π rad/s	T_s	50 μs	$\omega_{cpc}, \omega_{cvi}$	20π rad/s
L_i	350.45 μΗ	C_f	70 μF	L_g	34 μΗ
R_i	30 mΩ	R_f	2.1 Ω	R_g	1 mΩ
m_p	$\pi \times 10^{-6}$	n_q	9×10^{-4}	R_N	10 kΩ
K_{pv}	0.2475	Kiv	437.5	V_b^{in}	540 V
K_{pc}	3.0583	Kic	2668.8	V_{Db}	1.1 V
R_{lb}	1 mΩ	L_{lb}	300 μΗ	C_{dc}	10 mF
R_{onb}	2 mΩ	F_V	1	F_C	1
Z_{ld5}	(1.6+	K'_{pcb}	0.0034	K_{icb}^{\prime}	8.8188
Zld5	$j0.5024)~\Omega$				
Z_{ld6}	(1.6+	K'_{pvb}	4.6265	K'_{ivb}	606.0489
Zld6	$j0.5024)~\Omega$	n pvb		ivb.	
Z_{ld1}	(7+	Z_{ld2}	(14+	Z_{ld3}	(4.85 +
Ziai	$j2.198) \Omega$	Zld2	$j4.396) \Omega$	2183	$j1.4444) \Omega$
Z_{ld4}	(2.4+	Z_{ln14}	(0.1162 +	Z_{ln25}	(0.1356 +
Zld4	$j0.7536) \Omega$		$j0.0233) \Omega$		$j0.0271)~\Omega$
Z_{ln36}	(0.0969 +	Z_{ln45}	(0.0193 +	7	(0.0231 +
2/m36	$j0.0194) \Omega$	∠in45	$j0.0091) \Omega$	Z_{ln56}	$j0.011) \Omega$
$Z_{v,VSC1}$	(19.6 +	7 1/1/22	(0+	$Z_{v,VSC3}$	(38.7 +
Zv,VSC1	$j3.9) \mathrm{m}\Omega$	$Z_{v,VSC2}$	$j0)~\mathrm{m}\Omega$	2v, vsc 3	$j7.8) \mathrm{m}\Omega$

TABLE 2. Steady-state initial operating conditions.

Par.	Value	Par.	Value
δ_{01}	0 rad	V_{cd1},V_{cd2},V_{cd3}	[299,304,294] V
δ_{02}	$-3.6 \times 10^{-4} \text{ rad}$	$V_{cq1}, V_{cq2}, V_{cq3}$	[0.4,0,0.9] V
δ_{03}	$-2.99 \times 10^{-3} \text{ rad}$	$I_{id1}, I_{id2}, I_{id3}$	[180, 177, 184] A
$V_{gD1}, V_{gD2}, V_{gD3}$	[298,303,293] V	$I_{iq1}, I_{iq2}, I_{iq3}$	-[46,44,51] A
$V_{gQ1}, V_{gQ2}, V_{gQ3}$	-[1.5, 1.8, 1] V	$I_{gd1}, I_{gd2}, I_{gd3}$	[179, 177, 183] A
$V_{dc1}^{out}, V_{dc2}^{out}, V_{dc3}^{out}$	[800] V	$I_{gq1}, I_{gq2}, I_{gq3}$	-[55,53,60] A
$I_{b1}^{in}, I_{b2}^{in}, I_{b3}^{in}$	[152, 152, 153] A	D_{b1}, D_{b2}, D_{b3}	[0.326]
D_{d1}, D_{d2}, D_{d3}	[0.39, 0.39, 0.38]	D_{q1}, D_{q2}, D_{q3}	[0.02]
P_1, Q_1	[80.37, 24.88] kVA	P_2, Q_2	[80.47, 24.06] kVA
P_3, Q_3	[80.69, 26.78] kVA	I_{ldD1}, I_{ldQ1}	[38.7, -12.4] A
I_{lnD14}, I_{lnQ14}	[140.5, -42.8] A	I_{ldD2}, I_{ldQ2}	[19.7, -6.3] A
I_{lnD25}, I_{lnQ25}	[157.1, -46.5] A	I_{ldD3}, I_{ldQ3}	[55.3, -16.9] A
I_{lnD36}, I_{lnQ36}	[128, -43.4] A	I_{ldD4}, I_{ldQ4}	[106.6, -33.4] A
I_{lnD45}, I_{lnQ45}	[33.9, -9.5] A	I_{ldD5}, I_{ldQ5}	[159.5, -50] A
I_{lnD56}, I_{lnQ56}	[31, -6.6] A	I_{ldD6}, I_{ldQ6}	[159, -50] A

table compares the conventional PI-based controllers with the blended IPPI controllers as α changes. The closer a mode is to the right half of the complex plane, the larger its contribution towards the overall system performance. These modes are therefore considered the dominant modes in the system. An unstable mode m_{14}^{13} exists for $\alpha=1$ and $\alpha=0.6$, and would result in an unstable overall system performance. Not shown in the table are for $\alpha<0.6$, where the system remains unstable due to modes m_{14}^{13} and m_{16}^{15} as they move further into the right half of the complex plane. The other modes either remain fairly stationary or move further towards the right of the complex plane as α decreases from 0.9. An inference from Table 3 is that the modes are somewhat the furthest away from the right half of the complex plane at



 $\alpha=0.9$. This inference therefore demonstrates the need to select an appropriate blending factor α , that ensures modes that can impact stability are at their furthest possible locations from the right half of the complex plane. This provides an added flexibility in the scenario where conventional PI-based controllers (i.e. $\alpha=1$), are unable to ensure a stable overall system performance.

TABLE 3. Mode analysis at different blending factors.

m#	$\alpha = 1$	$\alpha = 0.9$	$\alpha = 0.8$	$\alpha = 0.7$	$\alpha = 0.6$
m_1	-4.29	-4.29	-4.29	-4.29	-4.29
m_2	-5.38	-5.38	-5.38	-5.38	-5.38
m_3	-55.61	-55.62	-55.64	-55.66	-55.68
m_4	-60.89	-60.89	-60.90	-60.91	-60.91
m_5	-62.75	-62.75	-62.75	-62.75	-62.75
m_6	-62.80	-62.80	-62.80	-62.80	-62.80
m_7	-62.80	-62.80	-62.80	-62.80	-62.80
m_8	-64.00	-64.00	-64.01	-64.02	-64.02
<i>m</i> ₉	-68.65	-68.67	-68.69	-68.71	-68.73
m_{10}	-73.65	-73.69	-73.72	-73.76	-73.79
m_{11}	-138.49	-133.36	-129.61	-126.68	-124.29
m_{12}	-175.67	-160.74	-152.53	-146.90	-142.65
13	5.30	-52.26	-26.06	-3.56	11.47
m_{14}^{13}	$\pm j706.59$	$\pm j509.00$	$\pm j400.81$	$\pm j343.13$	$\pm j305.73$
15	-4.80	-67.43	-42.04	-17.95	-1.29
m_{16}^{15}	$\pm j726.59$	$\pm j529.13$	$\pm j415.45$	$\pm j354.42$	$\pm j315.07$
17	-157.87	-157.88	-157.89	-157.90	-157.90
m_{18}^{17}	$\pm j130.55$	$\pm j130.51$	$\pm j130.47$	$\pm j130.44$	$\pm j130.40$
19	-165.42	-165.41	-164.82	-164.11	-163.44
m_{20}^{19}	$\pm j134.81$	$\pm j132.79$	$\pm j131.36$	$\pm j130.43$	$\pm j129.82$
21	-167.48	-166.41	-165.19	-164.18	-163.37
m_{22}^{21}	$\pm j133.60$	$\pm j131.25$	$\pm j130.03$	$\pm j129.37$	$\pm j128.98$
m_{24}^{23}	-212.72	-324.68	-214.97	-162.65	-131.76
¹¹¹ 24	$\pm j827.90$	$\pm j532.30$	$\pm j405.41$	$\pm j359.89$	$\pm j330.70$
,,,25	-216.94	-314.84	-205.32	-155.41	-125.79
m_{26}^{25}	$\pm j809.64$	$\pm j506.76$	$\pm j392.13$	$\pm j348.98$	$\pm j320.80$

In this study, the desired performance metrics σ_0 and ζ_0 are chosen to be -1000 and 0.1 respectively. Each particle's position $X_i = (\alpha_1, \alpha_2, \alpha_3)$ contain the parameters to be optimized. Analysis from Table 3 revealed the system is stable for $\alpha_{1,2,3} \in [0.68, 0.99]$. Further analysis revealed the domain of stability $\alpha_{1,2,3} \in [0.775, 0.962]$ satisfied $\zeta_m \ge 0.05$, whereas $\alpha_{1,2,3} \in [0.88, 0.912]$ satisfied $\zeta_m \ge 0.1$. Therefore to satisfy the condition limiting the maximum overshoot in (38) and improve the computational efficiency of the optimization framework, the domain of stability $\alpha_{1,2,3} \in [0.88, 0.912]$ is the updated constraint of the optimization. Following the steps describing the optimization framework using PSO in Section IV, the convergence of the objective function is shown in Fig. 9 and minimized at J = -13036 using (38). The resulting optimized blending factors, $\alpha = opt$ are $(\alpha_1 = 0.90244, \ \alpha_2 = 0.89974, \ \text{and} \ \alpha_3 = 0.88405).$ The corresponding locations and damping ratios for the modes of interest are shown in Table 4. The next subsection compares the dynamic performance of the optimized blending factors with $\alpha = 0.7$ that is on the margin of stability and the unstable scenario with conventional PI-based controllers where $\alpha = 1$.

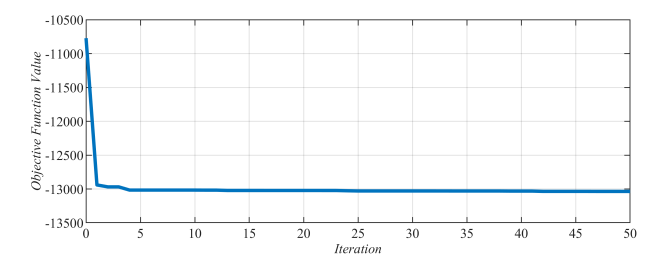


FIGURE 9. Objective Function Convergence.

TABLE 4. Mode locations and damping ratios using optimized blending factors.

$m_{\#}$	$\alpha = opt$	ζ_m
m_1	-4.29	1.00
m_2	-5.38	1.00
m_3	-55.63	1.00
m_4	-60.90	1.00
m_5	-62.75	1.00
m_6	-62.80	1.00
m_7	-62.80	1.00
m_8	-64.01	1.00
<i>m</i> 9	-68.67	1.00
m_{10}	-73.69	1.00
m_{11}	-133.36	1.00
m_{12}	-159.78	1.00
m_{14}^{13}	$-50.27 \pm j493.43$	0.1013
m_{16}^{15}	$-67.74 \pm j530.82$	0.1266
m_{18}^{17}	$-157.88 \pm j130.51$	0.7708
m_{20}^{19}	$-165.40 \pm j132.80$	0.7798
m_{22}^{21}	$-166.29 \pm j131.09$	0.7853
m_{24}^{23}	$-327.30 \pm j535.17$	0.5217
m_{26}^{25}	$-298.22 \pm j483.20$	0.5252

B. SIMULATION RESULTS

Simulation results presented within include start-up transient behavior and the (doubling) step change in the load at bus 6 at time = 0.2s. The response of the d-q components of the output VSC currents i_{idq} and the output VSC voltages v_{idq} from the DGs is shown in Fig. 10 for $\alpha = 0.7$ and in Fig. 11 for $\alpha = opt$. The dominant oscillatory mode m_{14}^{13} for $\alpha = 0.7$ (see Table 3) influences system performance due to its proximity to the right half of the complex plane, resulting in a long settling time. The desired dynamic performance is exhibited for $\alpha = opt$ (see Table 4) as the optimized blending factors move the dominant modes in the system to their furthest possible locations from the right half of the complex plane. In Fig. 11, for $\alpha = opt$, the steady-state values after the change in load are $i_{id1,2,3}$ [220.7, 218.8, 232.0] A, $i_{iq1,2,3}$ [-56.7, -56.3, -68.1] A, $v_{id1,2,3}$ [307.2, 311.5, 299.8] V, and $v_{iq1,2,3}$ [23.1, 22.1, 24.3] V.

The Figs. 12-15 and Figs. 16-19 illustrate the dynamic responses at the AC terminal of the VSC subsystem for conventional PI-based controllers ($\alpha = 1$) and optimized blended IPPI controllers ($\alpha = opt$) respectively. Both



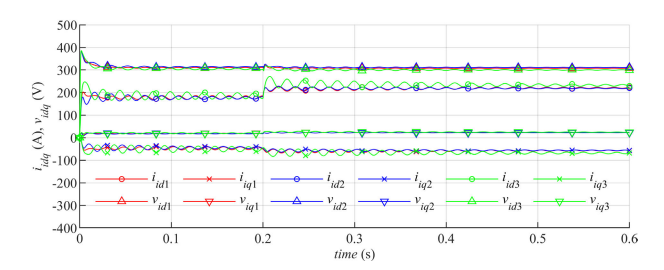


FIGURE 10. Output VSC Currents and Voltages from DGs for $\alpha = 0.7$.

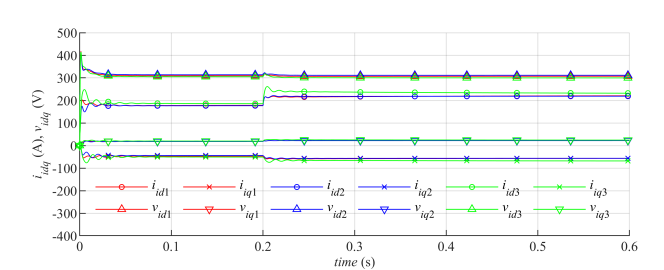


FIGURE 11. Output VSC Currents and Voltages from DGs for $\alpha = opt$.

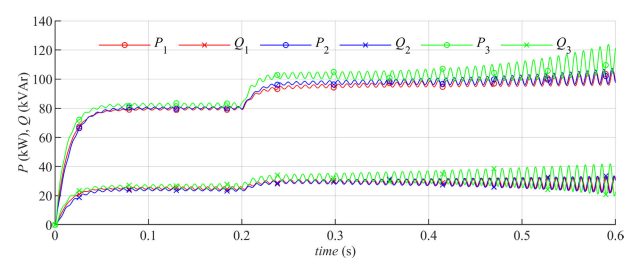


FIGURE 12. Active and Reactive Power Outputs from DGs for $\alpha = 1$.

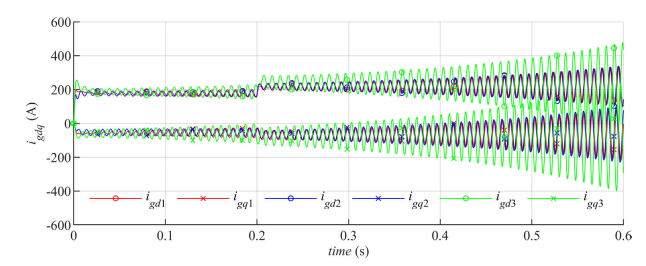


FIGURE 13. Injected Grid Currents from DGs for $\alpha = 1$.

scenarios illustrate the added flexibility and a more effective utilization of the VSC-interfaced DGs that is allowed when using blended IPPI voltage and current controllers. In the scenario where $\alpha=1$ (i.e. conventional PI-based controllers) the system is unstable due to the unstable mode m_{14}^{13} located in the right half of the complex plane (see Table 3). The Figs. 12, 13, 14, and 15 show responses of the active and reactive power outputs, the d-q components of the injected grid currents i_{gdq} , the d-q components of the output capacitor voltages v_{cdq} , and the droop-governed VSC frequency from the DGs respectively, illustrating the influence of this mode on overall system performance.

The desired dynamic performance is illustrated in the scenario where $\alpha = opt$ (i.e. optimized blended IPPI controllers) in which the dominant modes in the system are moved to their furthest possible locations from the right

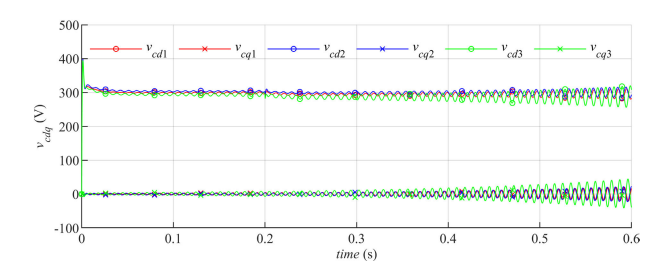


FIGURE 14. Output Capacitor Voltages from DGs for $\alpha = 1$.

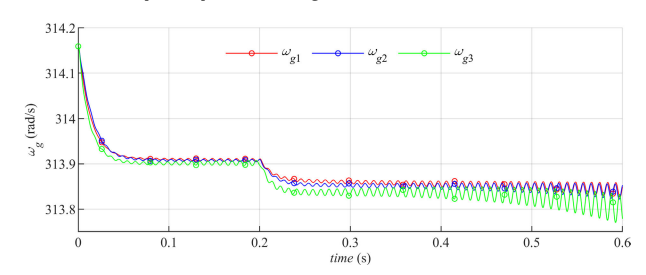


FIGURE 15. Droop-Governed VSC Frequency from DGs for $\alpha = 1$.

half of the complex plane. The response of the active and reactive power outputs from the DGs is shown in Fig. 16. The active (P) and reactive (Q) power loads in the MG network are shared between the DGs based on the droop control characteristics of the VSC's power controller together with its adjacent virtual impedance loop. The response of the DGs to the change in load is linked to its electrical distance from the changed load. The DG at bus 1 responds slower than the DG at bus 3 due to its longer electrical distance from bus 6 where the change in load occurred. The DG at bus 3 responds the fastest and initially provides most of the additional power to meet the change in load. The steady-state values after the change in load are $P_{1,2,3}$ [98.2, 98.6, 98.9] kW and $Q_{1,2,3}$ [29.3, 29.4, 33.6] kVar. The response of the d-q components of the injected grid currents i_{gdq} from the DGs is shown in Fig. 17. The d- and q- components respond in a similar manner to their corresponding active and reactive power outputs from the DGs. The steady-state values after the change in load are $i_{gd1,2,3}$ [220, 218, 232] A and $i_{gq1,2,3}$ [-66, -66, -78] A. The response of the d-q components of the output capacitor voltages v_{cdq} from the DGs is shown in Fig. 18. An inverse relationship exists between the d-component and the reactive power sharing between the DGs. The steady-state values after the change in load are $v_{cd1,2,3}$ [294, 299, 285] V and $v_{cq1,2,3}$ [0.4, 0, 1.2] V. The response of the droop-governed VSC frequency from the DGs is shown in Fig. 19. The larger the active power contribution from a DG during the change in load, the larger the deviation of its droop-governed frequency. The DG at bus 3 therefore has the largest swing compared to the other DGs. The steady-state network frequency after the change in load is 313.85 rad/s.

C. ANALYZING IMPACT ON DIFFERENT OPERATING CONDITIONS

The blended IPPI-based controllers using the optimized blending factors $\alpha = opt$ obtained, ($\alpha_1 = 0.90244$,

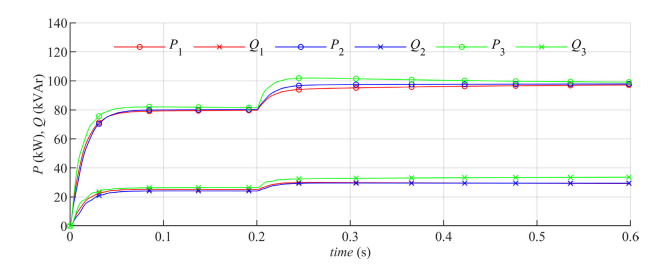


FIGURE 16. Active and Reactive Power Outputs from DGs for $\alpha = opt$.

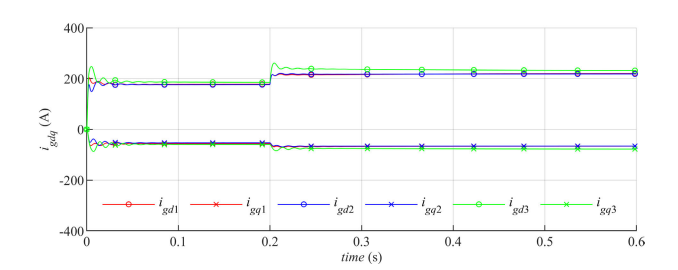


FIGURE 17. Injected Grid Currents from DGs for $\alpha = opt$.

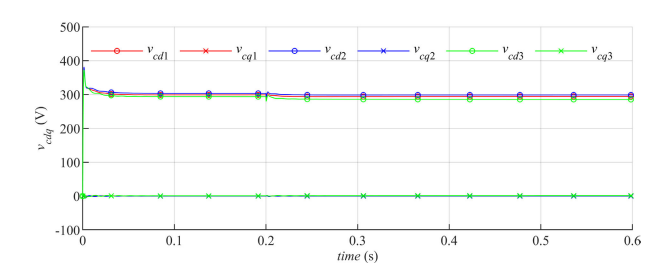


FIGURE 18. Output Capacitor Voltages from DGs for $\alpha = opt$.

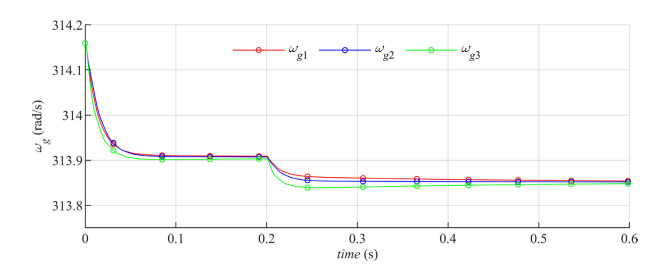


FIGURE 19. Droop-Governed VSC Frequency from DGs for $\alpha = opt$.

 $\alpha_2 = 0.89974$, and $\alpha_3 = 0.88405$), are analyzed under three different operating conditions (OCs), and the locations of the dominant modes $m_1 - m_{26}^{25}$ are compared with the conventional PI-based controllers (i.e. $\alpha = 1$) in Table 5. The parameters changed are with respect to base parameters in Table 1. OC 1 is a 10% reduction in network load and hence a reduction in DG power outputs ($P_{1,2,3}$ [74.40, 74.49, 74.69] kW and $Q_{1,2,3}$ [23.01, 22.23, 24.81] kVar). OC 2 uses dissimilar active power droop gains ($m_{p1,2,3}$ [0.9, 1, 1.1] × π × 10⁻⁶) resulting in different DG power outputs ($P_{1,2,3}$ [88.69, 80.07, 73.00] kW and $Q_{1,2,3}$ [22.28, 24.18, 29.33] kVar). In OC 2, the droop control characteristics shows an increase in active power output for the DG's VSC with the smaller m_p and a

TABLE 5. Mode analysis at different operating conditions.

OCs	OC 1		OC 2		OC 3	
m#	$\alpha = 1$	$\alpha = opt$	$\alpha = 1$	$\alpha = opt$	$\alpha = 1$	$\alpha = opt$
m_1	-4.39	-4.39	-4.27	-4.27	-4.96	-4.96
m_2	-5.49	-5.49	-5.35	-5.35	-6.20	-6.21
m_3	-55.47	-55.49	-55.77	-55.79	-56.04	-56.06
m_4	-60.92	-60.93	-60.91	-60.92	-60.89	-60.89
m_5	-62.76	-62.76	-62.75	-62.75	-62.76	-62.76
m_6	-62.80	-62.80	-62.80	-62.80	-62.80	-62.80
m_7	-62.80	-62.80	-62.80	-62.80	-62.80	-62.80
m_8	-63.90	-63.90	-64.07	-64.08	-64.03	-64.03
m ₉	-68.34	-68.37	-68.51	-68.54	-68.61	-68.64
m_{10}	-72.76	-72.79	-73.60	-73.64	-82.97	-83.04
m_{11}	-137.69	-132.72	-138.35	-133.24	-222.72	-187.63
m_{12}	-174.03	-158.85	-176.39	-160.22	-345.59	-221.65
m_{14}^{13}	12.65	-42.72	3.21	-51.39	35.90	-15.36
m_{14}	±j699.96	$\pm j493.89$	$\pm j707.62$	$\pm j493.04$	$\pm j693.36$	$\pm j485.77$
m_{16}^{15}	2.58	-59.11	-5.20	-68.69	23.00	-36.57
¹¹ 16	$\pm j719.23$	$\pm j530.19$	$\pm j727.20$	$\pm j530.92$	$\pm j714.88$	$\pm j520.85$
m_{18}^{17}	-157.62	-157.63	-157.87	-157.88	-157.57	-157.58
¹¹¹ 18	$\pm j130.38$	$\pm j130.35$	$\pm j130.54$	$\pm j130.50$	$\pm j130.30$	$\pm j130.26$
m_{20}^{19}	-165.16	-165.16	-165.57	-165.58	-165.73	-164.04
m ₂₀	$\pm j134.70$	$\pm j132.73$	$\pm j134.91$	$\pm j132.87$	$\pm j130.24$	$\pm j129.26$
m_{22}^{21}	-167.21	-166.08	-167.37	-166.13	-164.99	-163.14
m ₂₂	$\pm j133.56$	$\pm j131.07$	$\pm j133.50$	$\pm j131.03$	$\pm j127.62$	$\pm j127.87$
m_{24}^{23}	-210.98	-326.30	-213.99	-329.33	-215.27	-319.00
···24	$\pm j827.31$	$\pm j534.83$	$\pm j831.07$	$\pm j536.63$	$\pm j832.30$	$\pm j552.56$
m_{26}^{25}	-215.56	-297.39	-217.30	-295.60	-217.37	-292.30
¹¹¹ 26	$\pm j808.85$	$\pm j482.61$	$\pm j804.59$	$\pm j481.24$	$\pm j815.83$	$\pm j505.84$

decrease in the active power output for the DG's VSC with the larger m_p . OC 3 uses higher reactive power gains $(n_{q1,2,3}$ [2, 2, 2] \times 9 \times 10⁻⁴). In OC 3, a consequence of a higher n_q is a reduction in the output voltage of the VSCs and hence active and reactive power outputs $(P_{1,2,3}]$ [71.41, 71.42, 71.44] kW and $Q_{1,2,3}$ [22.20, 21.81, 23.17] kVar). The takeaway from Table 5 is that the modes m_{14}^{13} and m_{16}^{15} contributing to instability in the three different operating conditions when using PI-based control are at new stable locations when using IPPI-based control having appropriately selected blending factors. The optimized blending factors using one operating condition is sufficient for other operating conditions.

VI. CONCLUSION

Small-signal state-space models are developed in this paper for blended IPPI-based voltage and current controllers in a VSC to provide an added flexibility in the scenario where the conventional PI-based voltage and current controllers are unable to ensure a stable overall system performance. This translates to a more effective utilization of the VSC-interfaced DGs. To achieve a desirable dynamic performance, an optimization framework is developed utilizing particle swarm optimization to select appropriate blending factors. Within the optimization framework is an objective function proposed to enhance the damping characteristics and preserve stability through the resulting blending factors.



Time domain simulations are carried out to illustrate the responses of the DGs to a change in load. The analysis and results confirm the effectiveness of the optimization framework, the adequacy of the objective function, and the desired performance of the optimized blending factors.

REFERENCES

- [1] S. Sen and V. Kumar, "Microgrid modelling: A comprehensive survey," *Annu. Rev. Control*, vol. 46, pp. 216–250, Dec. 2018.
- [2] B. M. Eid, N. A. Rahim, J. Selvaraj, and A. Elkhateb, "Control methods and objectives for electronically coupled distributed energy resources in microgrids: A review," *IEEE Syst. J.*, vol. 10, no. 2, pp. 446–458, Jun. 2016.
- [3] C. Eyisi and Q. Li, "Load sharing scheme incorporating power security margins for parallel operation of voltage source inverters," *Energies*, vol. 14, no. 18, p. 5825, Sep. 2021.
- [4] M. Farrokhabadi, C. A. Cañizares, J. W. Simpson-Porco, E. Nasr, L. Fan, P. A. Mendoza-Araya, R. Tonkoski, U. Tamrakar, N. Hatziargyriou, and D. Lagos, "Microgrid stability definitions, analysis, and examples," *IEEE Trans. Power Syst.*, vol. 35, no. 1, pp. 13–29, Jan. 2020.
- [5] N. Pogaku, M. Prodanovic, and T. C. Green, "Modeling, analysis and testing of autonomous operation of an inverter-based microgrid," *IEEE Trans. Power Electron.*, vol. 22, no. 2, pp. 613–625, Mar. 2007.
- [6] I. P. Nikolakakos, H. H. Zeineldin, M. S. El-Moursi, and N. D. Hatziargyriou, "Stability evaluation of interconnected multi-inverter microgrids through critical clusters," *IEEE Trans. Power Syst.*, vol. 31, no. 4, pp. 3060–3072, Jul. 2016.
- [7] M. Naderi, Y. Khayat, Q. Shafiee, T. Dragicevic, H. Bevrani, and F. Blaabjerg, "Interconnected autonomous AC microgrids via back-toback converters—Part I: Small-signal modeling," *IEEE Trans. Power Electron.*, vol. 35, no. 5, pp. 4728–4740, May 2020.
- [8] B. Wang and G. Verbic, "Stability analysis of low-voltage distribution feeders operated as islanded microgrids," *IEEE Trans. Smart Grid*, vol. 12, no. 6, pp. 4681–4689, Nov. 2021.
- [9] F. Harashima and S. Kondo, "A design method for digital speed control system of motor drives," in *Proc. IEEE Power Electron. Specialists Conf.*, Jun. 1982, pp. 289–297.
- [10] F.-J. Lin, "Real-time IP position controller design with torque feedforward control for PM synchronous motor," *IEEE Trans. Ind. Electron.*, vol. 44, no. 3, pp. 398–407, Jun. 1997.
- [11] P. K. Nandam and P. C. Sen, "Analog and digital speed control of DC drives using proportional-integral and integral-proportional control techniques," *IEEE Trans. Ind. Electron.*, vol. IE-34, no. 2, pp. 227–233, May 1987.
- [12] T. Sreekumar and K. S. Jiji, "Comparison of proportional-integral (P-I) and integral-proportional (I-P) controllers for speed control in vector controlled induction motor drive," in *Proc. 2nd Int. Conf. Power, Control Embedded* Syst., Dec. 2012, pp. 1–6.
- [13] A. Chaoui, J.-P. Gaubert, and F. Krim, "Power quality improvement using DPC controlled three-phase shunt active filter," *Electric Power Syst. Res.*, vol. 80, no. 6, pp. 657–666, Jun. 2010.
- [14] F. Amrane, B. Francois, and A. Chaiba, "Experimental investigation of efficient and simple wind-turbine based on DFIG-direct power control using LCL-filter for stand-alone mode," ISA Trans., vol. 125, pp. 631–664, Jun. 2022.
- [15] S.-K. Sul, Control of Electric Machine Drive Systems. Hoboken, NJ, USA: Wiley, 2011.
- [16] W. S. Levine, Control System Fundamentals. Boca Raton, FL, USA: CRC Press, 2011.
- [17] A. Rodríguez-Cabero, M. Prodanovic, and J. Roldán-Perez, "Analysis of dynamic properties of VSCs connected to weak grids including the effects of dead time and time delays," *IEEE Trans. Sustain. Energy*, vol. 10, no. 3, pp. 1066–1075, Jul. 2019.
- [18] Y. Wang, X. Wang, F. Blaabjerg, and Z. Chen, "Harmonic instability assessment using state-space modeling and participation analysis in inverter-fed power systems," *IEEE Trans. Ind. Electron.*, vol. 64, no. 1, pp. 806–816, Jan. 2017.
- [19] B. Banković, F. Filipović, N. Mitrović, M. Petronijević, and V. Kostić, "A building block method for modeling and small-signal stability analysis of the autonomous microgrid operation," *Energies*, vol. 13, no. 6, p. 1492, Mar. 2020.

- [20] A. Rodríguez-Cabero, J. Roldán-Pérez, and M. Prodanovic, "Virtual impedance design considerations for virtual synchronous machines in weak grids," *IEEE J. Emerg. Sel. Topics Power Electron.*, vol. 8, no. 2, pp. 1477–1489, Jun. 2020.
- [21] J. L. Agorreta, M. Borrega, J. López, and L. Marroyo, "Modeling and control of *N*-paralleled grid-connected inverters with LCL filter coupled due to grid impedance in PV plants," *IEEE Trans. Power Electron.*, vol. 26, no. 3, pp. 770–785, Mar. 2011.
- [22] L. Herrera, E. Inoa, F. Guo, J. Wang, and H. Tang, "Small-signal modeling and networked control of a PHEV charging facility," *IEEE Trans. Ind. Appl.*, vol. 50, no. 2, pp. 1121–1130, Mar. 2014.
- [23] Q. Xu, N. Vafamand, L. Chen, T. Dragicevic, L. Xie, and F. Blaabjerg, "Review on advanced control technologies for bidirectional DC/DC converters in DC microgrids," *IEEE J. Emerg. Sel. Topics Power Electron.*, vol. 9, no. 2, pp. 1205–1221, Apr. 2021.
- [24] C. Eyisi and Q. Li, "Analysis and optimization of boost converter parameters in internal model-based control of voltage source converterbased ac microgrids," CSEE J. Power Energy Syst., early access, Sep. 8, 2023. [Online]. Available: https://ieeexplore.ieee.org/abstract/ document/10246138
- [25] Y. del Valle, G. K. Venayagamoorthy, S. Mohagheghi, J.-C. Hernandez, and R. G. Harley, "Particle swarm optimization: Basic concepts, variants and applications in power systems," *IEEE Trans. Evol. Comput.*, vol. 12, no. 2, pp. 171–195, Apr. 2008.



CHIEBUKA EYISI (Member, IEEE) received the B.Sc. degree in electrical/electronic engineering from the Kwame Nkrumah University of Science and Technology, Kumasi, Ghana, in 2010, and the M.Sc. degree in electrical engineering from the University of Central Florida, Orlando, FL, USA, in 2013. His research interests include power system optimization, renewable energy integration, and stability analysis of microgrids.



QIFENG LI (Senior Member, IEEE) received the Ph.D. degree in electrical engineering from Arizona State University, Tempe, AZ, USA, in 2016. He is currently an Assistant Professor with the Department of Electrical and Computer Engineering, University of Central Florida (UCF), Orlando, FL, USA. Before joining UCF Faculty, he held a position of a Postdoctoral Associate with the Department of Mechanical Engineering, Massachusetts Institute of Technology (MIT),

Cambridge, MA, USA, from 2016 to 2018. His research interests include convex optimization, uncertainty-aware optimization, and nonlinear systems with applications in power and energy systems.